Front. Struct. Civ. Eng. 2022, 16(3): 316–328
https://doi.org/10.1007/s11709-022-0810-8

RESEARCH ARTICLE

The damage evolution behavior of polypropylene fiber reinforced concrete subjected to sulfate attack based on acoustic emission

Ninghui LIANG[a,b*], Jinwang MAO[a,b], Ru YAN[a,c], Xinrong LIU[a,b], Xiaohan ZHOU[a,b]

[a] *School of Civil Engineering, Chongqing University, Chongqing 400045, China*
[b] *National Joint Engineering Research Center for Prevention and Control of Environmental Geological Hazards in the TGR Area, Chongqing University, Chongqing 400045, China*
[c] *PowerChina Chengdu Engineering Corporation Ltd., Chengdu 610072, China*
[*] *Corresponding author. E-mail: liangninghui0705@163.com*

ABSTRACT To study the damage evolution behavior of polypropylene fiber reinforced concrete (PFRC) subjected to sulfate attack, a uniaxial compression test was carried out based on acoustic emission (AE). The effect of sulfate attack relative to time and fiber hybridization were analyzed and the compression damage factor was calculated using a mathematical model. The changes to AE ringing counts during the compression could be divided into compaction, elastic, and AE signal hyperactivity stages. In the initial stage of sulfate attack, the concrete micropores and microcracks were compacted gradually under external load and a corrosion products filling effect, and this corresponded with detection of few AE signals and with concrete compression strength enhancement. With increasing sulfate attack time, AE activity decreased. The cumulative AE ringing counts of PFRC at all corrosion ages were much higher than those for plain concrete. PFRC could still produce AE signals after peak load due to drawing effect of polypropylene fiber. After 150 d of sulfate attack, the cumulative AE ringing counts of plain concrete went down by about an order of magnitude, while that for PFRC remained at a high level. The initial damage factor of hybrid PFRC was −0.042 and −0.056 respectively after 150 d of corrosion, indicating that the advantage of hybrid polypropylene fiber was more obvious than plain concrete and single-doped PFRC. Based on a deterioration equation, the corrosion resistance coefficient of hybrid PFRC would be less than 0.75 after 42 drying−wetting sulfate attack cycles, which was 40% longer than that of plain concrete.

KEYWORDS polypropylene fiber reinforced concrete, sulfate attack, damage evolution behavior, acoustic emission, damage factor

1 Introduction

Many concrete structures fail to reach their predetermined service life due to various non-mechanical failures [1,2], among which sulfate attack is one of the main ones. Expansion stress caused by chemical action and crystallization pressure caused by physical action are the main reasons for concrete cracking and destruction. The occurrence of microcracks also accelerates the deterioration of concrete structure performance [3,4]. The incorporation of fibers can enhance the concrete strength [5–8] and durability [9,10]. In recent years, polypropylene fiber (PF) has been widely used due to its advantages of light weight, low cost, good corrosion resistance and compatibility with concrete. Many scholars have studied the characteristics of polypropylene fiber reinforced concrete (PFRC), with fruitful results. The mixing of PF can significantly improve the tensile strength [11], impact resistance [12], crack resistance [13], fracture toughness [14], impermeability [15], and other properties of concrete.

Understanding concrete properties under load is

Article history: Received Oct 13, 2021; Accepted Dec 15, 2021

essential for assessing the stability and serviceability of buildings [16]. Determining the occurrence and development behavior of cracks is a primary task. Rabczuk and Belytschko [17,18] described a new approach for modelling discrete cracks using meshfree methods, which could be applied to 2D and the optimized model could be applied to 3D problems. The corresponding 2D and 3D computation agrees very well with the experimental data. Moreover, Rabczuk et al. [19] modeled the crack by separating particles located on opposite sides of the associated crack segments, thus developing a model that could be used in two- and three-dimensional problems in applied mathematics. Ren et al. [20] proposed an explicit phase field model for dynamic brittle fracture, which avoided the numerical difficulty in convergence and the calculation of anisotropic stiffness tensor in the implicit phase field model. Ren et al. [21] also proposed a higher order nonlocal operator method for the solution of boundary value problems, the method was used in the solution of phase field modeling of fracture. It can be seen that the research on computational studies capable of explaining the underlying physics has achieved fruitful results.

Acoustic emission is the technique capable of detecting, classifying, and locating damage in concrete by capturing and analyzing acoustic emission (AE) signals generated during the compression, splitting or other mechanical process [22]. This AE technique has been applied to study the damage of engineering materials [23]. Tetsuya et al. [24] found the relation between AE energy rate and physical properties and was correlated, thus the damage of concrete was qualitatively estimated in terms of AE parameters. Tetsuya et al. [25] also applied AE technique and damage mechanisms to quantitatively assess the damage to concrete structures. Wang et al. [26] studied the acoustic emission characteristics and damage process of polypropylene reinforced fiber mortars and steel fiber reinforced concrete at different strain rates. Their study has important value for the understanding of the characteristics of the damage evolution behavior of fiber reinforced concrete. Through comparing AE parameter characteristics of cementitious materials under bending and shear load, Alireza et al. [27] realized the fracture mode identification of tensile and shear cracking. Yuma et al. [28] applied continuous acoustic emission monitoring to the study of corrosion defects of reinforced concrete beams with wet−dry cycles, and determined the occurrence of corrosion and the nucleation of cracks caused by corrosion. The results show that AE technique has great prospects for quantitative evaluation of concrete corrosion caused by early corrosion expansion. It can be concluded that the AE signal is sensitive to the subtle damage inside materials and is suitable for composite materials damage analysis.

Regarding the damage evolution of PFRC, Qi et al. [29] derived a preliminary damage evolution equation based on the Moelands−Reinhardt single parameter power exponent constitutive equation and equivalent strain hypothesis. Xu et al. [30] identified the damage evolution behavior of HFRC using uniaxial cyclic compression and tension tests. Yang et al. [31] investigated the effects of mixing PF of different lengths or diameters and the effect of fiber size on the impact characteristics of concrete. The statistical damage model was used to obtain the damage degree D by fitting and analyzing their variation rules based on the statistical damage constitutive model and the particle swarm optimization algorithm. It can be seen that the research on damage evolution of PFRC has achieved fruitful results, but there are few reports on the damage evolution behavior of PFRC subjected to sulfate attack.

In this paper, the uniaxial compression test of PFRC subjected to sulfate attack was carried out based on AE technique, to study the damage evolution behavior inside concrete and reveal the effect of sulfate attack time and the effect of fiber hybridization. The damage factor evolution curve of PFRC subjected to sulfate attack was obtained using a mathematical model. The strength prediction model of PFRC subjected to sulfate attack was investigated by curve fitting based on compressive strength test results. It serves as an important guidance for the application of PFRC in sulfate attack environment.

2 Experiment

2.1 Materials and mixture design

The produced concrete was of strength grade C30. The structures of standard composite concrete and its control group consisted of the following materials: ordinary Portland cement as a binder; natural river sand as the fine aggregate (mud content is less than 2.1%, fineness modulus is 2.89); artificial gravel with two kinds of particle size (5−10 mm and 10−20 mm) as the main aggregate; polycarboxylate superplasticizer as water reducing agent; water for the mixing and curing of concrete; other additives including three different scales of PFs, two kinds of fine PFs (FPF1 and FPF2) and one kind of coarse polypropylene fiber (CPF). The physical and mechanical properties of FPF1, FPF2 and CPF are shown in Table 1, and Fig. 1 shows their appearance.

The preliminary experimental data [11–13,15] showed that the optimum single amount of FPF was 0.9 kg·m^{-3}, and that of CPF was 6 kg·m^{-3}. There are many factors affecting the performance of concrete and high variation in concrete compressive properties can be expected due to small changes in these parameters [32]. In order to reflect the function of fiber, the proportion of concrete mix was fixed, and only the content or mixing combination of PF was changed. 3 specimens were prepared for each sulfate

attack ages and a total of 162 cubic specimens were cast. The mix proportion of C30 PFRC is shown in Table 2.

The size of each concrete specimen was 100 mm × 100 mm × 100 mm. Figure 2 shows the fabrication and sulfate attack process of concrete specimens. Specimens were left in molds for 24 h, and finally cured in the curing room at (20 ± 2) °C and > 95% relative humidity for 28 d until tested. The dry−wet cycle was set as 7 d with a dry−wet ratio of 4:3. In wet cycle, concrete specimens were soaked in sodium sulfate solution with 10% mass fraction for 3 d continuously, and in dry cycle, all specimens were naturally dried for 4 d.

2.2 Acoustic emission method

2.2.1 Working principle of acoustic emission

In general, AE signals are stress waves caused by sudden strain releases due to internal fracture such as concrete cracking. When a material is overstressed, bursts of energy are released in the form of high-frequency sound waves originating in cracks or from plastic deformation [33]; strain energy is released and spread through the material in the form of elastic waves, which causes vibration on the monitored specimen surface. This kind of vibration on a concrete surface can be converted into voltage signals [16]. The signals are amplified and processed with equipment and displayed in the form of waveforms or AE ringing counts and other parameters, so that the characterization parameter information of the AE signal can be obtained. In this way, information about internal structure change of concrete can be obtained and the damage mechanism of material can be obtained by inversion method. Its working principle is shown in Fig. 3.

2.2.2 AE tests

The loading mode of the compressive test was by stress control first and then by displacement control. Initially, the loading rate was 0.3 MPa·s^{-1}. When the uniaxial load

(a) (b) (c)

Fig. 1 Appearance of PF. (a) FPF1; (b) FPF2; (c) CPF.

Table 1 Physical and mechanical properties of PF

fiber	diameter (μm)	length (mm)	tensile strength (MPa)	elastic modulus (GPa)	breaking elongation	density (g·cm^{-3})	recommended admixture (kg·m^{-3})
FPF1	26.1	19	641	10.6	26.0%	0.91	0.9
FPF2	100	19	472	5.8	19.9%	0.91	0.9
CPF	800	50	706	7.4	10.0%	0.95	6.0

Table 2 The mix proportion of C30 PFRC (kg·m^{-3})

group No.	PF content	cement	sand	coarse aggregate	water	fiber content	water-reducer
A0	–	380	701	1144	175	0	1%
A1	FPF1	380	701	1144	175	0.9	1%
A2	FPF2	380	701	1144	175	0.9	1%
A3	CPF	380	701	1144	175	6.0	1%
A4	FPF1 + CPF	380	701	1144	175	0.6 + 5.4	1%
A5	FPF1 + CPF	380	701	1144	175	0.9 + 5.1	1%
A6	FPF1 + CPF	380	701	1144	175	1.2 + 4.8	1%
A7	FPF1 + FPF2 + CPF	380	701	1144	175	0.45 + 0.45 + 5.1	1%
A8	FPF1 + FPF2 + CPF	380	701	1144	175	0.6 + 0.6 + 4.8	1%

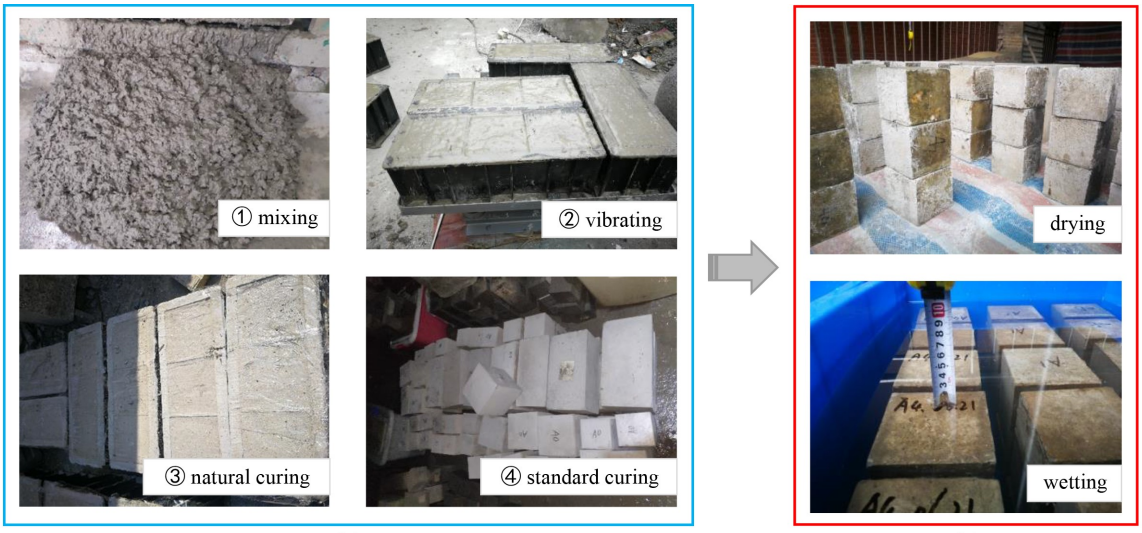

Fig. 2 The fabrication and sulfate attack process of concrete specimens: (a) fabrication of specimen; (b) dry−wet cycle (4:3).

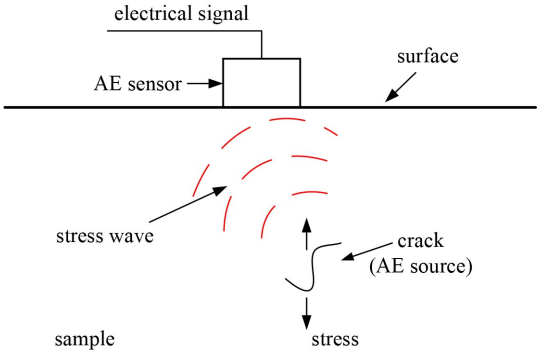

Fig. 3 Working principle of acoustic emission.

exceeded 40% of the estimated concrete compressive strength, the loading mode was changed to displacement control, and the loading rate was 0.5 mm·min^{-1} until the specimen failed. The DS2-8B AE testing system (Beijing Soft-land Times Scientific and Technology Co., Ltd) was adopted. The frequency range was set from 50 to 400 kHz. AE ringing counts were detected and recorded at the threshold level of 45 dB with a 40 dB gain in a pre-amplifier, and the sampling rate was 3 MHz. The system default settings were kept the same for other parameters. The AE signal acquisition process is shown in Fig. 4.

In order to avoid external interference and improve the quality of the AE signal, the contact surface between concrete specimens and AE sensors was polished and the center was cleaned with anhydrous ethanol. Petroleum jelly was applied as a coupling agent for the installation of sensors. Four AE sensors were attached on the four sides of each specimen, as shown in Fig. 5(a). In the initial stage of loading, no obvious cracks were found on the concrete surface, but after that, fine cracks paralleled to the load direction appeared. With increasing uniaxial load, the crack width increased and finally propagated throughout the specimen. When the uniaxial load reached the peak value, parts of the aggregates and mortar fell off, the bearing capacity decreased rapidly and the concrete failed completely, as shown in Fig. 5(b).

3 Result and discussion

3.1 Compressive strength

The relationship between compressive strength and sulfate attack ages is shown in Fig. 6, which shows that the compressive strength of plain concrete and PFRC can be divided into rising stage and falling stage during the corrosion time. The strength of plain concrete (A0) specimens increased within 0–60 d, while the increase in strength of PFRC continued for about 90 d. Then, the compressive strength of all specimens began to decrease.

Without sulfate attack, the compressive strength of group A0 was 32.49 MPa and the compressive strength of PFRC in each group was higher than that. The order was: hybrid PFRC > single doped PFRC > plain concrete. The strength of group A7 was the highest, which was 37.41 MPa. Compared with the compressive strength of A0, A7 increased by 15.1% and A8 increased by 13.5%. After 20 dry−wet cycle sulfate attack, the compressive strength of all PFRC specimens was higher than that of plain concrete, and the compressive strength of A8 was 40.21 MPa, which was the highest.

3.2 Variations of AE parameters

The acoustic emission characteristics of plain concrete (group A0) and PFRC (group A1, A2, A3, A6, and A8) subjected to sulfate attack for 0 and 150 d were investigated. The cumulative AE ringing count−time−load relationship is shown in Fig. 7. The load−time curve can reflect the change of the concrete bearing capacity in the

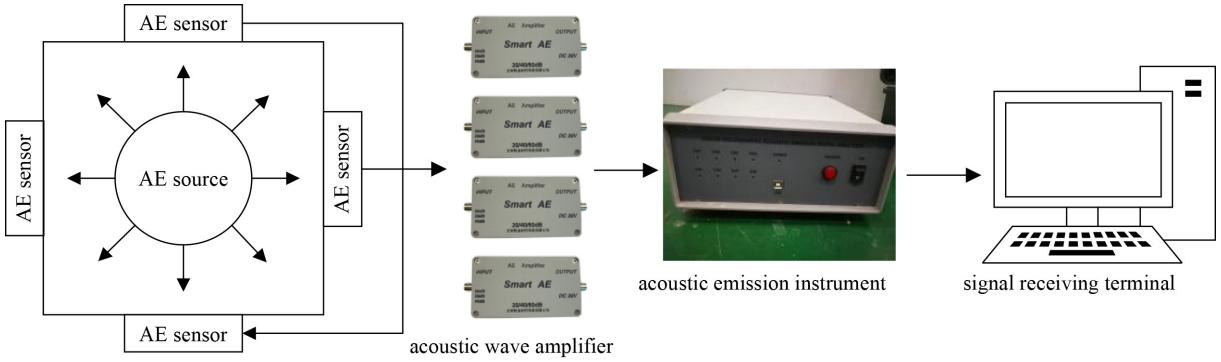

Fig. 4 Acquisition process of acoustic emission signal.

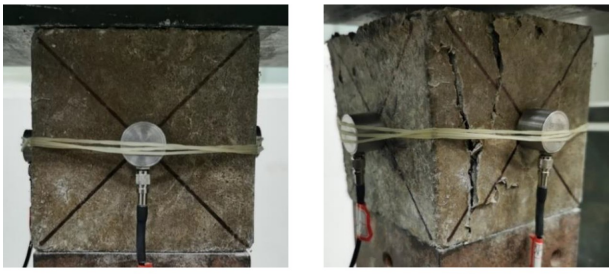

Fig. 5 Acoustic emission test. (a) Arrangement of AE sensors; (b) end of AE test.

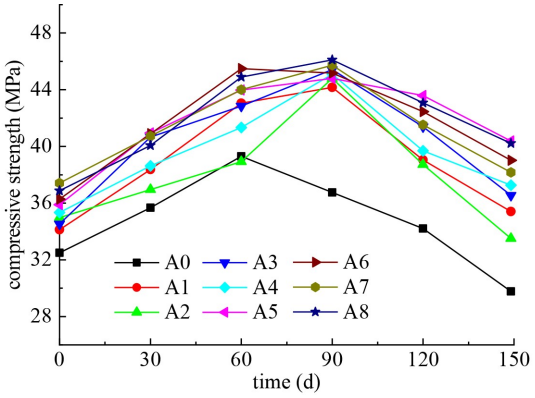

Fig. 6 Compressive strength of concrete at different corrosion ages.

compression test, and the AE ringing counts can reflect the change of AE activity during the process.

From above figures, the change of AE ringing counts could be divided into three stages in the loading process of plain concrete and PFRC.

In the initial stage of uniaxial compression test, all specimens showed similar behaviors. The load was initially low, approximately at a stress increment of 0%–15% f_{cu} (here f_{cu} denotes the compressive strength of the specimen), corresponding to low rate of detection of AE signals. This is because concrete inevitably contains a large number of micropores and micro-cracks. On one hand, the cement hydration reaction and bleeding of freshly mixed concrete may cause the bonding surface failure [34,35], then forming a large number of randomly distributed micro-cracks. On the other hand, concrete forms a large number of pore structures in the process of concrete hardening. Neither the presence of free water in the concrete matrix nor the air have been excluded completely as the main reasons for pore formation [36]. In this initial period, the original micropores and microcracks inside concrete were compacted gradually under uniaxial load, which changed the internal microstructure. The generated AE ringing counts were caused by the closure of original micro-cracks or micropores.

As uniaxial load increased, the concrete showed elastic behavior. The randomly distributed micro-cracks in the concrete matrix developed gradually with increasing stress. The cement particles inside concrete became dislocated, and new micro-cracks were generated. In this stage, AE activity was weak and the cumulative AE ringing counts increased slowly, which indicated that the micro-cracks were in a relatively stable stage. Because the strength of hardened cement is far less than that of aggregate, so that the propagation of cracks developed along the interfacial transition zone (ITZ) without large energy release. The micro-cracks propagation among cement and aggregate interface and the interconnectivity of large pores inside concrete were the main sources of AE signals.

The third stage was AE signal hyperactivity stage. The elastic behavior of the concrete changed to plastic behavior. At the beginning of the stage, AE activity and AE ringing counts increased suddenly. As the ultimate load approached, plenty of new cracks generated and the concrete deformation became increasingly larger, corresponded to the significant increase of AE signals and AE ringing counts, all of which were warning of the impending concrete failure. The residual strength enabled the specimen to continue loading. The macro cracks and deformation on the concrete surface were becoming increasingly larger. When the uniaxial load reduced to a certain level, AE activity decreased obviously. In this stage, AE signals were mainly derived from the formation and development of a large number of cracks.

3.3 Effect of sulfate attack time

When specimens were subjected to sulfate attack for 30 and 60 d, the cumulative AE ringing counts fluctuated, but the change range was small. During the whole loading process, the cumulative value of AE ringing counts was maintained about 10000 times, and the overall change trend was similar to that without sulfate attack. In the early stage of sulfate attack, the generation and propagation rate of cracks inside concrete decreased, corresponding to decrease in AE activity during the compaction stage. After 150 d sulfate attack, the cumulative AE ringing counts decreased significantly, especially for plain concrete, which decreased to about 1400 times or

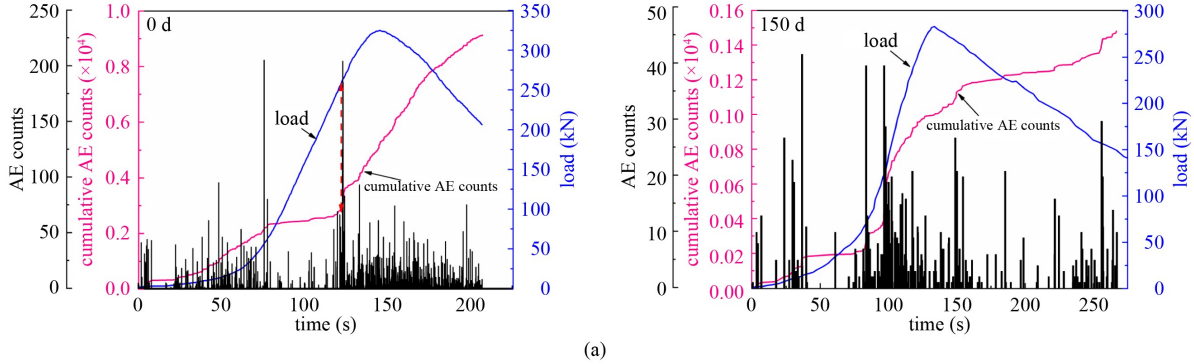

(a)

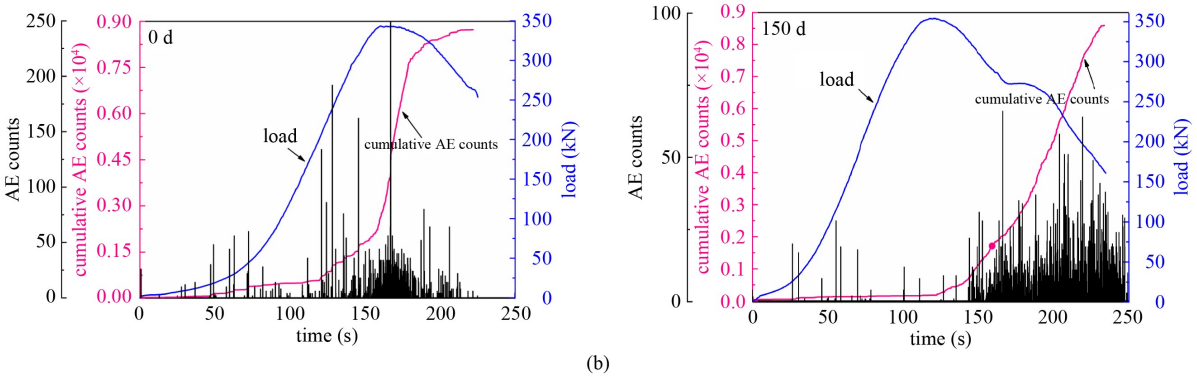

(b)

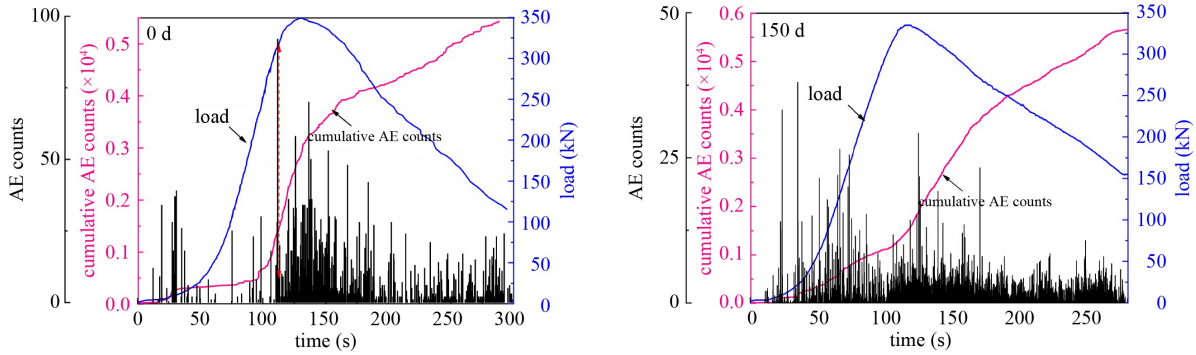

(c)

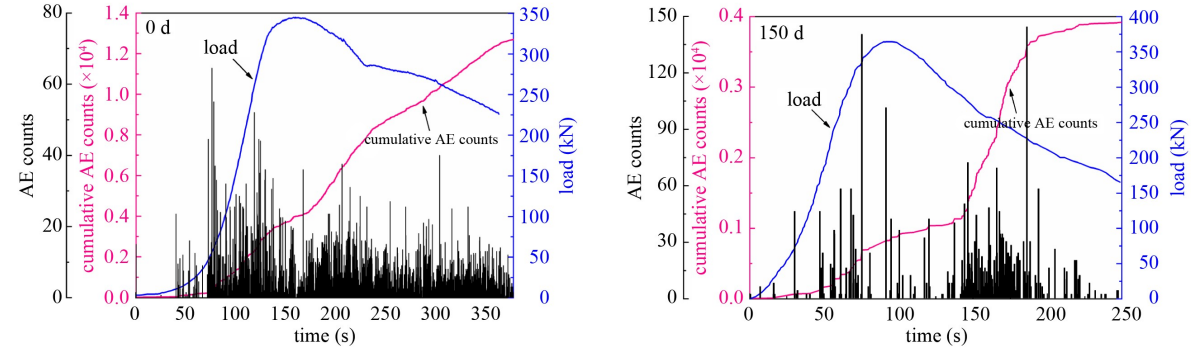

(d)

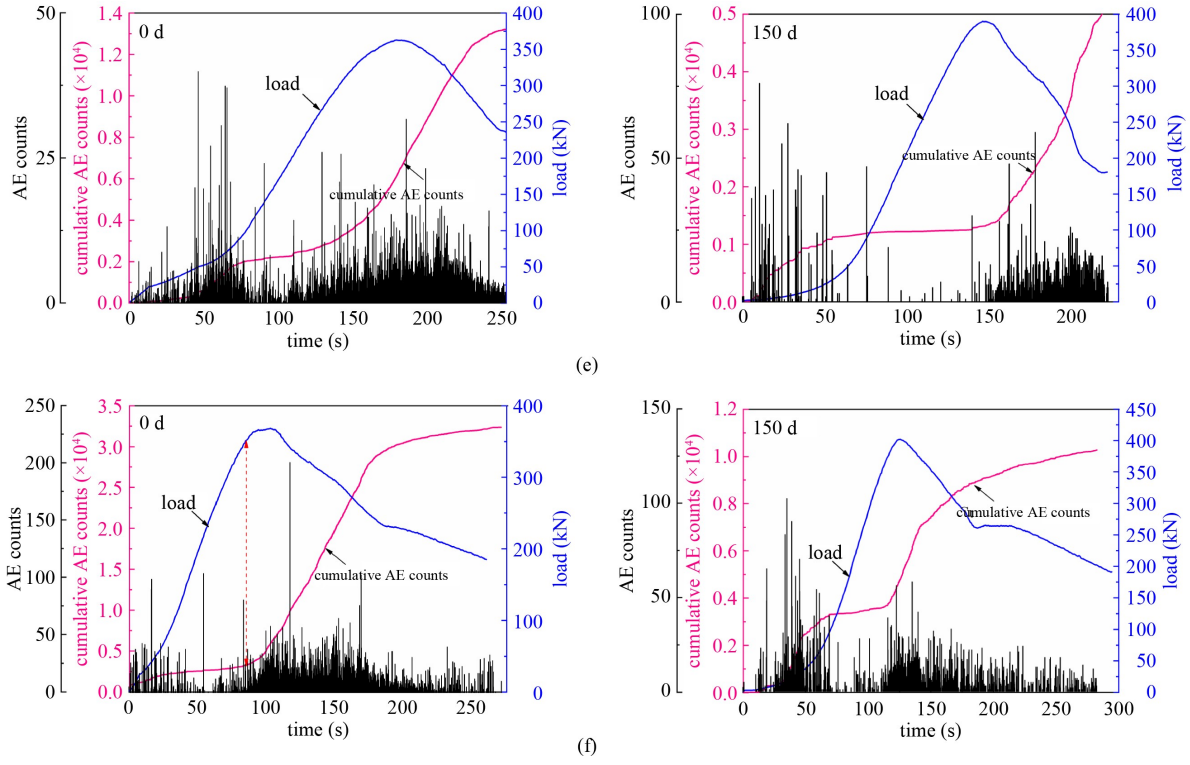

Fig. 7 AE ringing counts during uniaxial compression test at different sulfate attack ages. (a) corroded for 0 and 150 d of A0; (b) corroded for 0 and 150 d of A1; (c) corroded for 0 and 150 d of A2; (d) corroded for 0 and 150 d of A3; (e) corroded for 0 and 150 d of A6; (f) corroded for 0 and 150 d of A8.

about one order of magnitude. Additionally, the sharp increase point of cumulative AE ringing counts was also advanced. When compression load reached about 65% f_{cu}, AE activity increased sharply, corresponding to the appearance of macro cracks on concrete surface.

Under dry−wet cycles, sulfate ions diffuse into the concrete matrix through water pressure and capillary adsorption force [37]. Some of the sulfate ions react with dissolved calcium hydroxide (CH) in concrete to produce secondary gypsum ($C\bar{S}H_2$), as shown in chemical reaction equation (1). And the secondary gypsum, reacts with some calcium aluminate phases, such as tetracalcium aluminate (C_4AH_{13}), monosulfate ($C_4\bar{A}SH_{12}$) and tricalcium aluminate (C_3A), to form ettringite ($C_6A\bar{S}_3H_{32}$), as revealed in chemical reaction equation (2) [38].

$$CH(Ca^{2+} + 2OH^-) + SO_4^{2-} \rightarrow C\bar{S}H_2 + 2OH^- \quad (1)$$

$$\begin{cases} C_4AH_{13} + 3C\bar{S}H_2 + 14H \rightarrow C_6A\bar{S}_3H_{32} + CH \\ C_4A\bar{S}H_{12} + 2C\bar{S}H_2 + 16H \rightarrow C_6A\bar{S}_3H_{32} \\ C_3A + 3C\bar{S}H_2 + 26H \rightarrow C_6A\bar{S}_3H_{32} \end{cases} \quad (2)$$

Corrosion products and sulfate crystallization filled pores inside concrete, so that concrete compacted gradually and the porosity decreased. Therefore, AE activity in the compaction stage was weak and the concrete compressive strength improved. With sulfate attack time increasing, the micro-cracks developed when the expansion stress of corrosion products or sulfate crystallization stress was greater than the concrete tensile strength. In addition, the hardened cement paste was consumed and the bonding between cement and aggregate reduced so that the number of internal cracks increased, resulting in the decline of concrete strength. Therefore, the longer the sulfate attack time became, the faster the generation and expansion of internal cracks was. Eventually, interconnected macro cracks formed and the concrete matrix loosened, corresponding that the longer sulfate attack the concrete suffered, the lower AE activity would be obtained in the whole loading process.

3.4 Effect of fiber hybridization

Figure 7 suggests that the cumulative AE ringing counts of PFRC also showed an attenuation tendency with increase in the sulfate attack time. But compared with plain concrete, the attenuation of PFRC cumulative AE ringing counts was delayed. AE activity of PFRC was higher than that of plain concrete at all sulfate attack ages. After 150 d sulfate attack, the cumulative AE ringing counts of PFRC remained at a high level.

Comparing the cumulative AE ringing count-time relationship curves of specimens without sulfate attack, one can see that AE activity of PFRC was lower in the early stage of the compressive test. This was due to the crack resistance of PF, which made the formation and

expansion of micro-cracks inside concrete slower [13]. The incorporation of PF delayed the growth mutation point of PFRC cumulative AE ringing counts and the point occurred at about 75%f_{cu}, meaning that PFRC could carry more load before it entered the plastic stage. The porosity of PFRC was slightly higher than that of plain concrete due to the addition of PF [15]. However, the incorporation of PF optimized the concrete pore structure, reducing the connectivity of the concrete internal pores and increasing the tortuosity of permeability path. This reduced the rate of SO_4^{2-} invasion into concrete. PFRC retained better mechanical properties than plain concrete under the action of sulfate attack. Additionally, PF was dispersed evenly inside concrete [12], which greatly improved the concrete integrity. The interfacial bond strength between fiber and concrete was significantly affected by the embedded lengths and angles from a concrete matrix [39]. In the loading process, FPF alleviated the effects of grown-in microcracks to a certain extent, while CPF was more effective in inhibiting the development of macro cracks [14] indicating that the hybridization of different scales of PF optimized concrete properties during the entire crack propagation process. After the concrete specimen was destroyed, multiple fibers between cracks could be seen, the fibers pulled together the concrete matrix, as shown in Fig. 8(a). Usually, the FPF was broken due to its lower bearing capacity, while one end of the CPF was pulled out and the other end was firmly embedded in the concrete matrix indicating that the adhesive capacity between PF and concrete matrix was good. The bridging effect of PF optimized the brittleness and improved the toughness of concrete specimens. AE sensors received the signals of PF being stretched and pulled out in the compression process, as shown in Fig. 8(b). Therefore, the AE signals from PFRC were dense and abundant, which was one of the main reasons why the cumulative AE ringing counts of PFRC was much higher than that of plain concrete.

4 Damage factor

Taking cumulative AE ringing counts as the variable indicating extent of damage, and combining corrosion damage and load damage with the mathematical model it was possible to study the damage evoluation behavior of PFRC subjected to sulfate attack. In the loading process, the internal flaws of the material generated and developed. Kachanov defined the damage variable as follows [40]:

$$D = \frac{A_d}{A}, \tag{1}$$

where A_d is the total area of damage zone and A is the cross-sectional area of concrete in the undamaged state.

When concrete is undamaged, $D = 0$. When concrete loses its bearing capacity completely, $D = 1$. It is assumed that the cumulative AE ringing counts is N_m when the whole section A is destroyed completely under undamaged condition. The cumulative AE ringing counts of per unit area is N_c.

$$N_c = \frac{N_m}{A}. \tag{2}$$

When the damage area takes an area of A_d, the cumulative AE ringing counts N_d is given by:

$$N_d = N_c A_d = \frac{N_m}{A} A_d. \tag{3}$$

According to Eqs. (2) and (3), it can be found that:

$$D = \frac{N_d}{N_m}, \tag{4}$$

when the loading of the specimen stops, the cumulative AE ringing counts is recorded as N_m.

The state after sulfate attack is taken as the first damage state and the second damage state is caused by loading after corrosion. According to the extended Lemaitre strain equivalence principle [41], the damage constitutive relation under load of PFRC subjected to sulfate attack can be shown by Eq. (5):

$$\sigma = E_t(1 - D)\varepsilon, \tag{5}$$

where D is damage factor and E_t is the elastic modulus of PFRC after sulfate attack. Taking the total damage variable as D_T, the stress-strain relationship of PFRC under corrosion and loading is shown by Eqs. (6) and (7):

$$\sigma = E_0(1 - D_T)\varepsilon, \tag{6}$$

$$D_T = D_t + D - D_t D, \tag{7}$$

where D_t is concrete damage caused by sulfate attack, D is concrete damage caused by load, $D_t D$ is concrete damage caused by corrosion-load coupling.

From the compressive test results, we could see that the cubic compressive strength of PFRC specimens decreased with corrosion time increasing. In order to reflect the

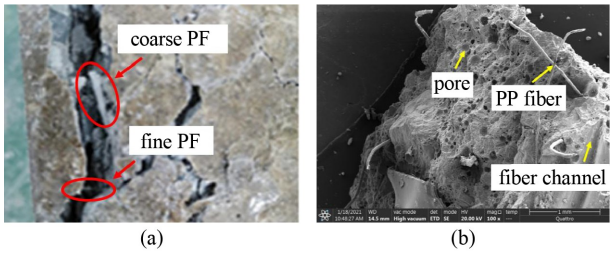

Fig. 8 Function of PF. (a) Pulling effect of PF; (b) fibers pulled out.

deterioration degree of concrete better, the elastic modulus of each group of specimens was selected as damage variable. Therefore, the concrete damage caused by sulfate attack was:

$$D_t = 1 - \frac{E_t}{E_0}. \tag{8}$$

According to Eqs. (4), (7), and (8), the damage evolution equation of PFRC subjected to sulfate attack can be shown by Eq. (9):

$$D_T = 1 - \frac{E_t}{E_0}\frac{N_m - N_d}{N_m}. \tag{9}$$

When only corrosion damage is considered, the cumulative AE ringing counts $N_d = 0$ and $D_T = D_t$; When only load damage is considered, $E_t = E_0$ and $D_t = D$. Figure 9 shows the damage evolution curve of plain concrete and PFRC under different corrosion ages (0, 90, 120, and 150 d), which can be calculated by Eq. (9).

Figure 9 suggests that concrete is damaged due to sulfate attack. At the initial stage of corrosion, the compressive strength of concrete specimens improves to a certain extent (the damage factor in Fig. 9 is negative), which is consistent with the compressive testing results. The concrete initial damage develops with sulfate attack time increasing. The initial damage factor of plain concrete (A0) was 0.025 at 120 d sulfate attack, and increased to 0.107 with corrosion at 150 d. Obviously, the initial damage of PFRC occurred later than that of plain

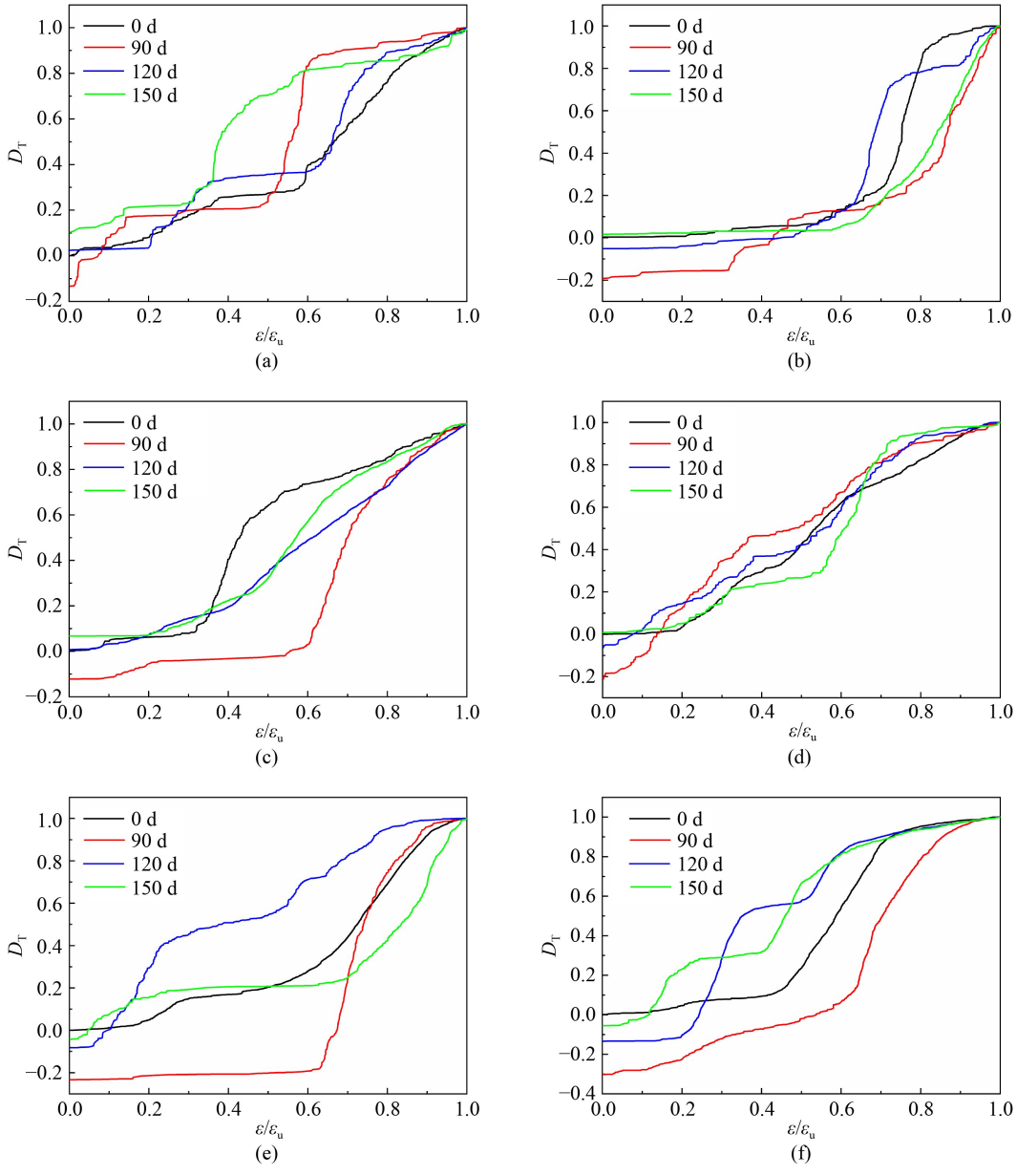

Fig. 9 Damage evolution curves of concrete under sulfate attack and uniaxial loading. (a) A0; (b) A1; (c) A2; (d) A3; (e) A6; (f) A8.

concrete. For the single doped PFRC, A1, A2, and A3, the damage factors were greater than 0 when at about 150 d of sulfur attack, at 0.017, 0.067, and 0.008, respectively. While hybrid PFRC (A6 and A8) was still less than 0 after 150 d sulfate attack, the initial damage factor was −0.042 and −0.056, respectively, which was much lower than plain concrete and single-doped PFRC. It was observed that the incorporation of PF delayed the concrete damage rate caused by sulfate attack effectively and the advantage of hybrid PF was more obvious than single-doped PF, which was consistent with the AE testing results. This indicated that this mathematical model can reflect the damage evolution behavior of plain concrete and PFRC subjected to sulfate attack well.

5 The deterioration equation of PFRC compressive strength

Based on the results of the compressive strength test, the strength prediction model of PFRC subjected to sulfate attack was investigated by curve fitting. It is assumed that S_0 is the compressive strength of concrete subjected to standard curing for 28 d without sulfate attack, S_n is the compressive strength of concrete compressive strength after n cycles (30 d is considered as 4 cycles) of drying and wetting, and λ_0 is the deterioration constant. The deterioration equation of PFRC compressive strength can be shown by Eq. (10) [42]:

$$\frac{\mathrm{d}S_n}{\mathrm{d}n} = -\lambda_0(S_n - S_0). \tag{10}$$

According to Eq. (10), it can be found that:

$$\frac{S_n}{S_0} = \mathrm{e}^{-\lambda_0 n} + C. \tag{11}$$

When $n = 0$, $S_n/S_0 = 1$, corresponding to $C = 0$. The final solution of the deterioration equation can be obtained as:

$$K = \frac{S_n}{S_0} = \mathrm{e}^{-\lambda_0 n}, \tag{12}$$

where K is the corrosion resistance coefficient of compressive strength.

The compressive strength of plain concrete and PFRC can be divided into rising stage and falling stage with corrosion time increasing. Assuming that $\lambda(n) = \lambda_0 n$, $\lambda(n)$ varies with sulfate attack time. Any function can be expressed by a polynomial, so it can be assumed that:

$$\lambda(n) = A + Bn + Cn^2 + Dn^3 + \cdots. \tag{13}$$

where B, C, D,..., are undetermined coefficient. Equation (13) should satisfy the following boundary conditions:

1) when $n = 0$, $K = 1$, and $K \to 0$ when $n \to \infty$;

2) in the interval $[0,n]$, $K \geqslant 0$;

3) there is only one point where the first derivative of the deterioration equation is equal to 0;

4) in the interval $[0,n]$, the second derivative of the deterioration equation is less than 0.

According to the above boundary conditions, the fundamental form of the deterioration equation is shown as Eq. (14):

$$K = \mathrm{e}^{Bn+Cn^2}. \tag{14}$$

Equation (14) is used to fit the compressive strength test result of PFRC subjected to drying−wetting cycle sulfate attack. The test data and deterioration fitting curve were shown in Fig. 10.

The fitting results show that the correlation coefficient R^2 is always greater than 0.9 except for A2, indicating that the deterioration equation can fit the compressive strength of PFRC subjected to sulfate attack well, which could be used to predict the strength of PFRC after sulfate attack. The concrete durability specification [43] rules the concrete has suffered severe sulfate attack when the concrete corrosion resistance coefficient is lower than 0.75. According to the deterioration equation, the corrosion resistance coefficient of A0 would be less than 0.75 after 30 drying−wetting cycles. That period of PFRC is longer than that of A0, especially hybrid PFRC A6 and A8, the corrosion resistance coefficient of A6 and A8 would be less than 0.75 after 42 drying−wetting cycles. In terms of corrosion resistance coefficient, it could be seen that the addition of PF makes the service life of PFRC about 40% longer than that of plain concrete under sulfate attack conditions.

6 Conclusions

This paper studied the AE activity characteristics during the uniaxial compression of PFRC subjected to sulfate attack and analyzed the effect of sulfate attack time and fiber hybridization. The concrete damage factor evolution curve was obtained with a mathematical model and the deterioration equation of PFRC subjected to sulfate attack was investigated by a fitting curve. The main conclusions were as follows.

1) The observed AE ringing counts could be divided into three stages. The first stage was compaction stage, during which there were few AE signals, with a stress level of 0%–15%f_{cu}. The second stage was an elastic stage, during which micro-cracks in concrete matrix generated and developed gradually. The third stage was AE signal hyperactivity stage, during which cracks inside concrete developed rapidly and intensively when the stress reached about 75%f_{cu}.

2) In the early stage of sulfate attack, micropores inside concrete were filled by corrosion products and sulfate

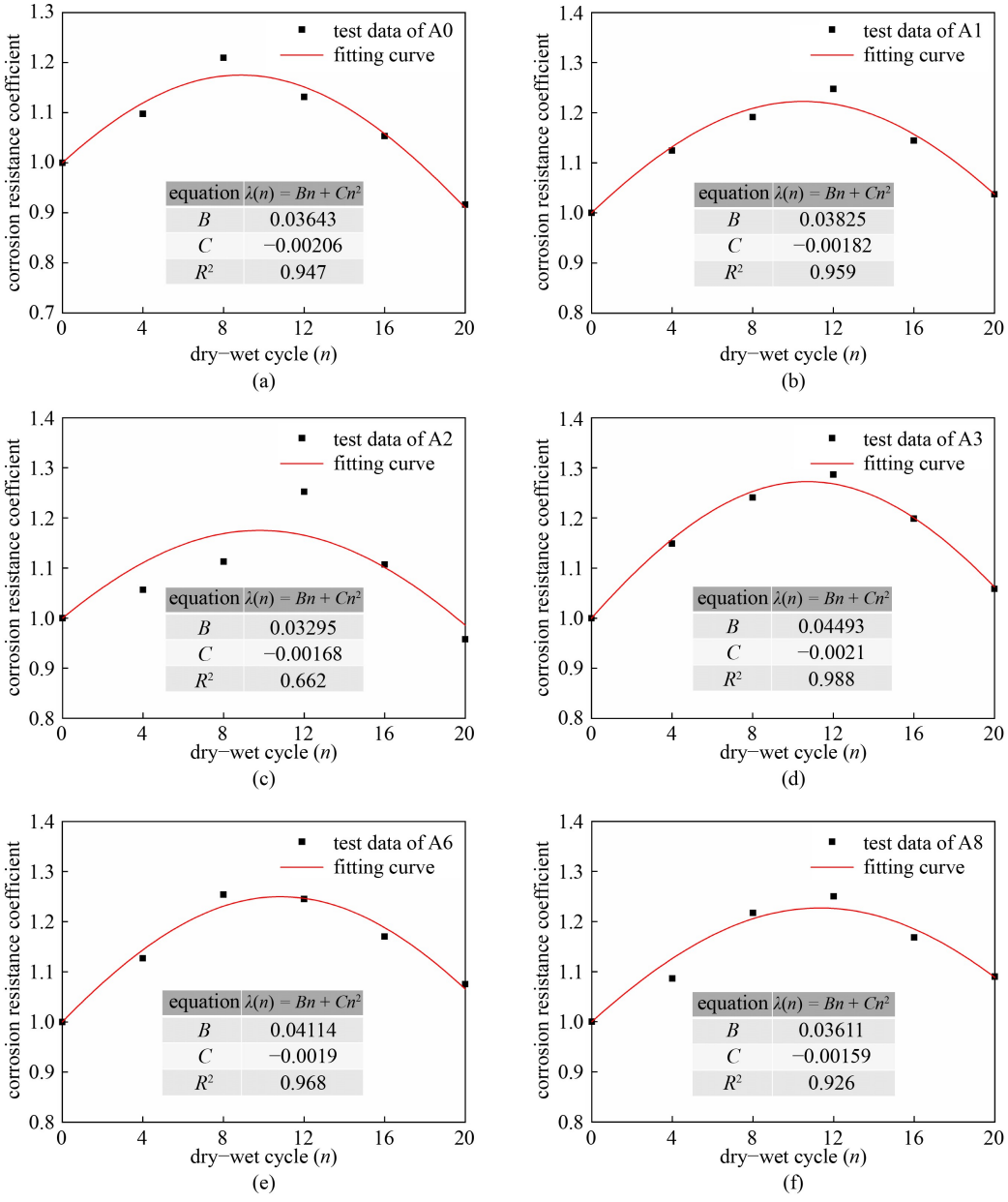

Fig. 10 The compressive strength deterioration fitting curve of PFRC subjected to sulfate attack. (a) A0; (b) A1; (c) A2; (d) A3; (e) A6; (f) A8.

crystallization, and the concrete compressive strength improved. With sulfate attack time increasing, the cohesiveness between cement and aggregate decreased, the matrix structure became loose and concrete strength decreased, corresponded the lower AE activity in the whole loading process.

3) The incorporation of PF could improve the toughness of concrete and AE activity of PFRC at all sulfate attack ages was much higher than that of plain concrete. Compared with plain concrete, the attenuation of PFRC cumulative AE ringing counts was delayed. Before peak loading, the anti-cracking mechanism of fibers made the formation and expansion of micro-cracks slower. Due to the drawing effect of PF, PFRC still had a long period of AE activity after peak loading.

4) The initial damage factor D_T was negative in all groups at 90 d sulfate attack. A0 increased to 0.025 after 120 d corrosion. After 150 d sulfate attack, the initial damage factor of A1, A2, and A3 was greater than 0, while A6 and A8 was still less than 0. This showed that the incorporation of PF, especially hybrid PF could improve the sulfate resistance of concrete. The deterioration equation can fit the compressive strength of PFRC subjected to sulfate attack. According to the equation, the addition of PF makes the service life of PFRC about 40% longer than that of A0 under sulfate attack conditions.

Future research should focus on the two- [17] and three-dimensional [18,19] stress states of specimens,

which is more consistent with common stress states of concrete structures.

Acknowledgements The support from Mechanical Effect and Safety Analysis of Severely Damaged Tunnel Renovation Process (No. H20210058) is gratefully acknowledged. The authors declare that they have no known competing financial interests or personal relationships that could have appeared to influence the work reported in this paper.

References

1. Liu Y M, Yu H M, Wang C, Wang C L. Research on mechanism of damage of anhydrock in dolomite layer to tunnel structure. Rock and Soil Mechanics, 2011, 32(9): 2704−2708
2. Xing Z S, Deng M, Wang A G, Liu K W. Internal sulfate attack on concrete caused by gypsum-bearing aggregates. Journal of Building Materials, 2014, 17(1): 30−34
3. Raphael I T, Barzin M. Modeling of damage in cement-based materials subjected to external sulfate attack. II: Comparison with experiments. Journal of Materials in Civil Engineering, 2003, 15(4): 314−322
4. Zuo X B, Sun W. Full process analysis of damage and failure of concrete subjected to external sulfate attack. Journal of the Chinese Ceramic Society, 2009, 37(07): 1063−1067
5. Meng K, Xu L H, Chi Y. Experimental investigation on the mechanical behavior of hybrid steel-polypropylene fiber reinforced concrete under conventional triaxial cyclic compression. Construction & Building Materials, 2021, 291: 123262
6. Holovata Z, Kirichenko D, Korneeva I, Neutov S, Vyhnanets M. Experimental studies of fiber-reinforced concrete under axial tension. Materials Science Forum, 2021, 6266: 323−329
7. Hugo C, João P C R, Pimienta P. Flexural strength at high temperatures of a high strength steel and polypropylene fiber concrete. Construction & Building Materials, 2019, 227: 116721
8. Yang J, Chen B C, Nuti C. Influence of steel fiber on compressive properties of ultra-high performance fiber-reinforced concrete. Construction & Building Materials, 2021, 302: 124104
9. Qin Y, Duan M H, Ma W L, Li Y L, Zhou H. Experimental study on the damage permeability of polypropylene fiber-reinforced concrete. Construction & Building Materials, 2021, 286: 122592
10. Wang J H. The study of steel fiber reinforced concrete durability based on damage mechanics. Research Journal of Applied Sciences, Engineering and Technology, 2014, 7(3): 543−550
11. Liang N H, Liu X R, Sun J. Uniaxial tensile test of multi-scale polypropylene fiber reinforced concrete. Journal of Chongqing University, 2012, 35(6): 80−84
12. Liu X R, Ke W, Liang N H, Miao Q X, Yang P. Study on the dynamic mech anical properties of concrete multi size polypropylene fiber based on SHPB test. Materials Reports, 2018, 32(S1): 484−489
13. Liang N H, Liu X R, Sun J. Experimental study of crack resistance for multi-scale polypropylene fiber reinforced concrete. Journal of China Coal Society, 2012, 37(8): 1304−1309
14. Liang N H, Dai J F, Liu X R, Zhong Z L. Experimental study on the fracture toughness of concrete reinforced with multi-size polypropylene fibers. Magazine of Concrete Research, 2019, 71(9): 468−475
15. Guo Z. Experimental study on the impermeability of multi-scale polypropylene fiber concrete. Thesis for the Master's Degree. Chongqing: Chongqing University, 2018
16. Geng J S, Sun Q, Zhang Y C, Cao L W, Zhang W Q. Studying the dynamic damage failure of concrete based on acoustic emission. Construction & Building Materials, 2017, 149: 9−16
17. Rabczuk T, Belytschko T. Cracking particles: A simplified meshfree method for arbitrary evolving cracks. International Journal for Numerical Methods in Engineering, 2004, 61(13): 2316−2343
18. Rabczuk T, Belytschko T. A three-dimensional large deformation meshfree method for arbitrary evolving cracks. Computer Methods in Applied Mechanics and Engineering, 2007, 196(29−30): 2777−2799
19. Rabczuk T, Zi G, Bordas S, Nguyen-Xuan H. A simple and robust three-dimensional cracking-particle method without enrichment. Computer Methods in Applied Mechanics and Engineering, 2010, 199(37−40): 2437−2455
20. Ren H L, Zhuang X Y, Anitescu C, Rabczuk T. An explicit phase field method for brittle dynamic fracture. Computers & Structures, 2019, 217: 45−56
21. Ren H L, Zhuang X Y, Rabczuk T. A higher order nonlocal operator method for solving partial differential equations. Computer Methods in Applied Mechanics and Engineering, 2020, 367: 113132
22. Trąmpczyński W, Goszczyńska B, Bacharz M. Acoustic emission for determining early age concrete damage as an important indicator of concrete quality/condition before loading. Materials (Basel), 2020, 13(16): E3523
23. Jiao Y B, Zhang Y, Guo M, Zhang L D, Ning H, Liu S Q. Mechanical and fracture properties of ultra-high performance concrete (UHPC) containing waste glass sand as partial replacement material. Journal of Cleaner Production, 2020, 277: 123501
24. Tetsuya S, Saki N, Yuma S, Tomoki S, Masayasu O. Damage estimation of concrete canal due to freeze and thawed effects by acoustic emission and X-ray CT methods. Construction & Building Materials, 2020, 245: 118343
25. Tetsuya S, Masayasu O, Mitsuhiro S. Relative damage evaluation of concrete in a road bridge by AE rate-process analysis. Materials and Structures, 2007, 40(2): 221−227
26. Wang Y, Chen S J, Ge L, Zhou L, Hu H X. Analysis of dynamic tensile process of fiber reinforced concrete by acoustic emission technique. Journal of Wuhan University of Technology-Materials Science Edition, 2018, 33(5): 1129−1139
27. Alireza F, Anastasios C M, Theodore E M, Hamidreza F, Dimitrios G A. Fracture mode identification in cementitious materials using supervised pattern recognition of acoustic emission features. Construction & Building Materials, 2014, 67: 129−138
28. Yuma K, Tomoyo W, Tomoe K, Masayasu O. Corrosion mechanisms in reinforced concrete by acoustic emission. Construction & Building Materials, 2013, 48: 1240−1247
29. Qi F, Yang B, Li X B. Research on damage evolution of polypropylene fiber concrete under splitting load. Advances in

Building Materials, 2011, 1278: 287−291
30. Xu L H, Wei C M, Li B. Damage evolution of steel-polypropylene hybrid fiber reinforced concrete: Experimental and numerical investigation. Advances in Materials Science and Engineering, 2018, 2018: 1719427
31. Yang X, Liang N H, Liu X R, Zhong Z L. A study of test and statistical damage constitutive model of multi-size polypropylene fiber concrete under impact load. International Journal of Damage Mechanics, 2019, 28(7): 973−989
32. Hamdia K M, Silani M, Zhuang X Y, He P F, Rabczuk T. Stochastic analysis of the fracture toughness of polymeric nanoparticle composites using polynomial chaos expansions. International Journal of Fracture, 2017, 206(2): 215−227
33. Alireza F, Salamone S, Bismarck L, Andrew W. Acoustic emission monitoring of a reinforced concrete shear wall by *b*-value-based outlier analysis. Structural Health Monitoring—An International Journal, 2013, 12(1): 3−13
34. Zhang J, Han Y D, Gao Y. Effects of water-binder ratio and coarse aggregate content on interior humidity, autogenous shrinkage, and drying shrinkage of concrete. Journal of Materials in Civil Engineering, 2014, 26(1): 184−189
35. Hong J Y, Jae H K, Hyo-Gyoung K. Experimental simulation of bleeding under a high concrete column. Cement and Concrete Research, 2014, 57: 61−69
36. Chen Y L, Shao W, Zhou Y C. Elastoplastic damage constitutive model of water-saturated concrete under uniaxial compression. Engineering Mechanics, 2011, 28(11): 59−63
37. Yan Y D, Jin W L, Wang H L, Lu C H. Chloride transport in cracked concrete under wet-dry cycling condition. Journal of Central South University, 2013, 44(5): 2060–2067 (in Chinese)
38. Yin G J, Zuo X B, Tang Y J, Olawale A, Wang J L. Numerical simulation on time-dependent mechanical behavior of concrete under coupled axial loading and sulfate attack. Ocean Engineering, 2017, 142: 115−124
39. Vrijdaghs R, Di Prisco M, Vandewalle L. Short-term and creep pull-out behavior of polypropylene macrofibers at varying embedded lengths and angles from a concrete matrix. Construction & Building Materials, 2017, 147: 858−864
40. Liu B X, Huang J L, Wang Z Y, Liu L. Study on damage evolution and acoustic emission character of coal-rock under uniaxial compression. Chinese Journal of Rock Mechanics and Engineering, 2009, 28(S1): 3234−3238
41. Li X P, Lu Y N, Wang Y J. Research on damage model of single jointed rock masses under coupling action of freeze−thaw and loading. Chinese Journal of Rock Mechanics and Engineering, 2013, 32(11): 2307−2315
42. Wang H Y, Qiu W G, Du L F, Gong L. Durability prediction model for tunnel lining concrete under sulfate corrosion. Modern Tunnelling Technology, 2014, 51(3): 91−97
43. Ministry of Housing and Urban-Rural Development of the People's Republic of China. Standard for Design of Concrete Structure Durability, GB/T 50476-2019. Beijing: China Architecture and Building Press, 2019 (in Chinese)